Diffusive intertwining of two fluid phases in chemically patterned microchannels

Olga Kuksenok,[1] David Jasnow,[2] and Anna C. Balazs[1]
[1]*Department of Chemical Engineering, University of Pittsburgh, Pittsburgh, Pennsylvania 15261, USA*
[2]*Department of Physics and Astronomy, University of Pittsburgh, Pittsburgh, Pennsylvania 15261, USA*
(Received 16 July 2003; published 25 November 2003)

Via a coarse-grained model, we simulate the flow of a pressure driven binary AB fluid through a three-dimensional microchannel, which is decorated on both top and bottom with distinct A- and B-like patches. The advection is ''frustrated'' because A-like patches are placed in the path of the B stream and similarly, B-like patches are placed in the path of the A fluid. A competition between two factors, the advection caused by the imposed flow and the interactions between the confined fluids and the patterned substrates, introduces nonlinearity into the system. This nonlinear behavior gives rise to a temporally periodic state, where the A and B fluids are intertwined. In effect, the simple pattern of chemically distinct patches introduces positive feedback, which is responsible for the instability of the interface separating the injected fluids.

DOI: 10.1103/PhysRevE.68.051505 PACS number(s): 64.75.+g, 05.70.Np, 05.70.Ln

I. INTRODUCTION

The idea that flowing fluids can intertwine to form ''braids,'' ''knots,'' or other entanglements has fascinated scientists for decades. Such topologically complicated structures can occur in high Reynolds number flow [1]. In this paper, we simulate a coarse-grained model for a binary system to isolate an example of complex intertwining and temporally periodic patterns at low Reynolds number. This behavior occurs when parallel streams of two immiscible fluids, A and B are driven through a three-dimensional microchannel that is decorated with chemically distinct patches on both the top and bottom walls. In particular, B-like (A-like) patches are placed in the path of the incoming A (B) fluid stream. The B-like (A-like) patches preferentially attract the B (A) fluid. The competition between the advection from the imposed flow and the interactions between the confined fluid and the patterned substrate introduces nonlinearity into the reduced dynamical system. We find that this nonlinearity gives rise to the periodic formation of complex interpenetrating spatial structures at the center of a microchannel. Downstream from the patches, these structures are periodic in space and oscillatory in time, and may be regarded as traveling waves.

The observed phenomenon happens even in the absence of hydrodynamic interactions (i.e., solely with imposed flow). In addition, we take the densities and viscosities of both the fluids to be equal. Therefore, the instability of the fluid interfaces observed here is different from classical fluid instabilities (i.e., Rayleigh-Taylor, Kelvin-Helmholtz instabilities, or viscous fingering) [2].

We note that this surface pattern of chemical patches (see Fig. 1) was chosen because it is one of the simplest designs for introducing preferential wetting interactions that could perturb the fluid flow in the system. Furthermore, the particular pattern of an A-like patch next to a B-like region can readily be fabricated on the micron scale. Through various techniques, researchers have in fact produced even more complicated checkerboard patterns on these length scales [3,4].

This specific case is representative of a broader class of systems, namely, driven fluids that flow past chemically heterogeneous or patterned surfaces. Such systems can be found in nature [5] and in fabricated devices, where chemical patterning is used, for example, to control the flow and reaction of fluids in microfluidic instruments and biosensors [6]. There have, however, been very few theoretical studies on the behavior of fluid mixtures that are driven past domains with preferential wetting [7–9]. Thus, there has been little exploration of the rich dynamical behavior that can occur when there is a coupling between advection and selective interactions with the patterned substrate. From a fundamental point of view, such studies can reveal novel morphological instabilities in these dynamical systems [9]. From a technological aspect, the findings can be used to design microfluidic and nanofluidic devices, where the solubilization and transport of biologically relevant molecules without significant contamination or dispersion are of great importance [5]. As we show below, our system provides a means of creating ''sluglike'' flow in microchannels, where well-defined A and B domains are formed at the outlet periodically in time. Consequently, we believe that this system can be highly useful in microfluidic applications.

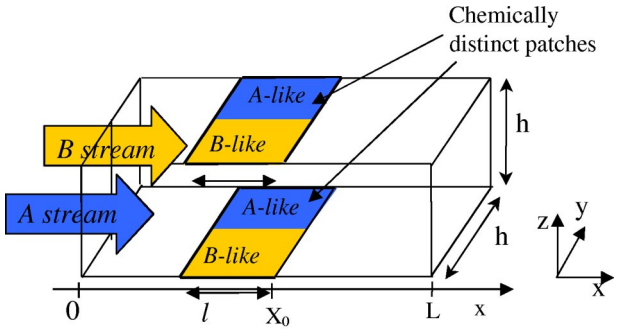

FIG. 1. (Color online) Schematic of system. Chemically modified patterns are the same on the top and bottom substrates and consist of A-like and B-like patches. At the inlet of the channel ($x=0$), we have two-stream flow. Dark gray (blue in the color version) represents A fluid; light gray (yellow in the color version) represents B fluid.

II. THE MODEL

An imposed pressure gradient drives two immiscible fluids, A and B, to flow through the microchannel shown in Fig 1. Both the top and bottom of this microchannel are decorated with adjacent A- and B-like patches; the A-like patch has a preferential attraction for the A component and likewise, the B patch has an affinity for B. Note that at the inlet, the A-like patch is placed in the path of the B fluid, and the B-like patch lies in the path of the A stream. The patches on the top and bottom of the channel are identical to, and lie in registry with, each other.

To characterize the morphology of the fluid, we define an order parameter $\varphi(\vec{r},t)=\rho_A(\vec{r},t)-\rho_B(\vec{r},t)$ where $\rho_i(\vec{r},t)$ represents the local number density of the *ith* component, i =A,B. The thermodynamic behavior of the system is assumed to be described by the free energy functional $F=F_0+\Psi_S$, where F_0 is the Ginzburg-Landau free energy for a binary mixture [10] given by

$$F_0=\int d\vec{r}\left[-\frac{a}{2}\varphi^2+\frac{b}{4}\varphi^4+\frac{\kappa}{2}|\vec{\nabla}\varphi|^2\right]. \quad (1)$$

We consider the fluid to be in the two-phase coexistence regime $(a,b,\kappa>0)$, where the equilibrium order parameter for the A/B phase is $\varphi_{A/B}=\pm\varphi_{eq}$, $\varphi_{eq}=\sqrt{a/b}$. The term $(\kappa/2)|\vec{\nabla}\varphi|^2$ represents the free energy cost of forming order parameter gradients, in particular, interfaces between the A and B fluid phases. The second term in the free energy functional, Ψ_s, represents a wall potential that describes the interaction between a fluid element at the point $\vec{r}$ and the patterned substrate. Specifically, we take [12]

$$\Psi_s=\int d\vec{r}\int d\vec{s}\{\tfrac{1}{2}V(\vec{s})e^{-|\vec{r}-\vec{s}|/r_0}[\varphi(\vec{r})-\tilde{\varphi}(\vec{s})]^2\}, \quad (2)$$

where the inner integral represents integration over the substrates. $V(\vec{s})=V=$const on the patterns and is zero otherwise, and r_0 represents the range of the substrate potential. We choose $\tilde{\varphi}(\vec{s})=\varphi_{A(B)}$ for $\vec{s}$ on the A(B) patches. Through Eq. (2), the free energy F is reduced when the fluid is A rich (B rich) near the A-like (B-like) patches.

The evolution of the order parameter for this system is taken to be described by the Cahn-Hillard equation [10,13]:

$$\frac{\partial\varphi}{\partial t}+\vec{u}\cdot\vec{\nabla}\varphi=M\nabla^2\mu, \quad (3)$$

where $\mu=\delta F/\delta\varphi$ is a chemical potential and M is the mobility of the order parameter, taken to be constant. The velocity field $\vec{u}$ obeys the Navier-Stokes equation in the overdamped limit (appropriate for low Reynolds number or creep flow) [10]:

$$0=-\vec{\nabla}p-\vec{\nabla}P+\eta\nabla^2\vec{u}+\mu\vec{\nabla}\varphi. \quad (4)$$

Here, η is the shear viscosity of the fluid, taken to be constant for both phases, $\vec{\nabla}P$ is the constant imposed pressure gradient along the channel, and p is a Lagrange multiplier that guarantees the incompressibility condition, $\vec{\nabla}\cdot\vec{u}=0$.

To rewrite Eqs. (3) and (4) in dimensionless units, we choose a characteristic length scale ξ and a time scale $\tau_0=\xi^2/aM$, which is equal to the diffusion time for order parameter fluctuations through the distance ξ. The order parameter value is normalized by φ_{eq}. It should be noted that, normally, in investigations of phase separation in infinite volumes, the most appropriate choice for the characteristic length is the thickness of the interface, $\xi_{int}=\sqrt{\kappa/a}$ [13]. In this study, we consider fluids with different interfacial properties while keeping the size of the channel constant; therefore, we do not scale length with ξ_{int}. Rather we choose ξ as proportional to the channel width h. For convenience, we introduce a dimensionless parameter $\tilde{\kappa}=\xi_{int}^2/\xi^2$, in terms of which the interfacial tension is expressed as $\sigma\sim\kappa\varphi_{eq}^2/\xi_{int}\sim\varphi_{eq}^2a\xi\sqrt{\tilde{\kappa}}$ [11]. In practice, we control interfacial properties by changing $\tilde{\kappa}$. Equations (3) and (4) can now be rewritten as

$$\frac{\partial\varphi}{\partial t}+\vec{u}\cdot\vec{\nabla}\varphi=\nabla^2\mu, \quad (5)$$

$$0=-\vec{\nabla}p+\nabla^2\vec{u}+\vec{H}+C\mu\vec{\nabla}\varphi, \quad (6)$$

where $\vec{H}=-\vec{\nabla}P\tau_0\xi/\eta$ is the dimensionless form of the imposed pressure gradient. We assume that the pressure gradient is applied along the x axis, so that only the x component of the vector $\vec{H}$ is nonzero, $H_x\equiv H$. [Note that in Eqs. (5) and (6), as well as in the following text, for simplicity, we have used the same symbols for the dimensionless values $\mu,\varphi,\vec{\nabla},t,\vec{u}$, etc., as we used in the dimensional equations (1)–(4).]

The last term in Eq. (6) represents the hydrodynamic interactions, or, in other words, the osmotic force that is due to changes in the order parameter distribution. The constant $C=\sigma\xi/D\eta\sqrt{\tilde{\kappa}}$ depends on the fluid properties (interfacial tension σ, diffusivity $D=aM$, and viscosity η) and defines the importance of hydrodynamic interactions in the system. If $C\ll1$, for example, in the case of high viscosity fluids, it may be possible to neglect hydrodynamic interactions. In this case, there is no backflow in the system, and the velocity along the x axis, u_x, has an undistorted Poiseuille profile that is a solution of $\nabla^2u_x+H=0$. In this paper, we only consider situations where we can neglect hydrodynamic interactions and set C equal to zero. We have, in fact, carried out calculations for moderate values of C ($C<20$) for the fixed value $H=6\times10^{-6}$ and found qualitatively similar results to those reported here. It should be noted, however, that for $C<20$, the distortions of the velocity field (due to gradients in the order parameter) are at least an order of magnitude smaller than the maximum values of the imposed velocities. On the other hand, in bulk systems with no mean flow, $C\approx20$ is sufficiently large to modify the scaling behavior of domain growth from that found strictly without hydrodynamics ($C=0$). For higher values of C (i.e., $C>20$), the observed periodic behavior becomes unstable. The results of these

simulations will be reported in a subsequent paper where we will discuss in more detail the influence of hydrodynamic interactions.

The following boundary conditions are imposed on the walls of the channel: $\partial\mu/\partial n|_{wall}=0$, $\partial\varphi/\partial y|_{y=0,h}=0$, and $\partial\varphi(\vec{s})/\partial z|_{z=0,h}=\pm\tilde{k}^{-1}\int d\vec{s}_i\{V(\vec{s}_i)[\varphi(\vec{r})-\tilde{\varphi}(\vec{s}_i)]\}|_{\vec{r}\to\vec{s}}$, where "+" is taken at $z=0$ and "−" is taken at $z=h$. The last condition arises explicitly from the minimization of free energy in the presence of the substrate potential. At the entry of the channel, we have two-stream flow; at the exit, we assume free draining flow, i.e., $\partial\varphi/\partial x|_{x=L}=0$. For the velocity field, we assume no-slip boundary conditions on all walls [14].

To update the value of φ in Eq. (5), we use a cell dynamical system method [15]. In the simulations described below, we initially set the dimensionless parameters of the system to the following values: l, the length of patch, is 20, the simulation box size is 140×30×30, and the interaction parameters are $r_0=3$, $V=0.01$ [16]. In the graphical output of the simulations, the A fluid is shown in blue and the B fluid is shown in yellow.

III. RESULTS AND DISCUSSION

Our goal is to analyze the morphology of the fluid as it flows through the channel shown in Fig. 1. In the discussion below, we first describe the salient features of the system, highlighting the necessary conditions for observing the oscillatory patterns. We then provide a scaling analysis that allows us to relate the properties of the interpenetrating structure to the characteristics of the fluid and the imposed pressure gradient.

At the onset of the simulations, two parallel streams of fluid A and B are driven by a constant pressure gradient to move through this channel. The patches strongly perturb the morphology in the channel. The cost in free energy for having each component near its respective nonwettable patch is sufficiently high that the fluid from the A stream diffuses across the channel to the A-like patch and similarly the B fluid diffuses to the B-like patch. At early times ($t<10^3$ for all the simulations presented here), the initial diffusion towards the A (B) patches plays the dominant role until the thickness of the A (B) fluid layer on the appropriate patches is at least equal to r_0. For later times, when the A (B) patches are covered by an A (B) fluid layer of thickness $\approx r_0$, the spatiotemporal dynamics are determined by a competition between advection caused by the imposed pressure gradient and diffusional relaxation towards the thermodynamic equilibrium state (which would be reached in the absence of advection) [see Fig. 2(a)].

For relatively low velocities ($H\ll H_1=2.6\times10^{-4}$ for the parameters chosen here), the fluid mainly mimics the structure of the underlying pattern and an imposed flow causes only small distortions in the thermodynamically determined distribution of φ. Under these conditions, our chosen pattern of patches primarily leads to a diffusive switching of the A-rich and B-rich regions. In other words, downstream from the patterned region, the position of the A and B fluid regions is reversed with respect to that at the inlet of the channel. For the higher velocities, but still lower than H_1, the morphology is more complicated, but we always observe a time-independent steady state.

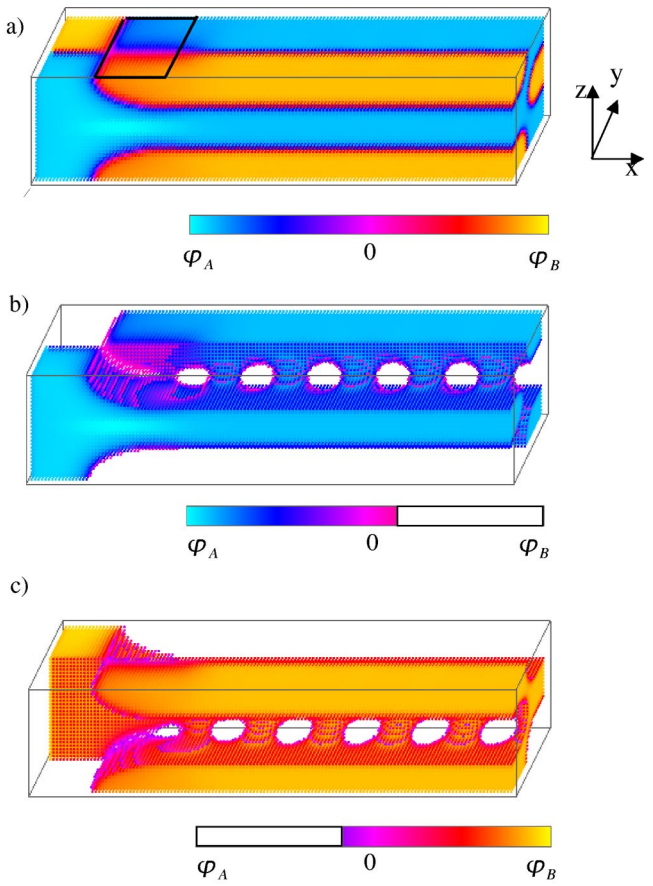

FIG. 2. (Color online) Order parameter distribution at $t=6\times10^4$ time steps; $H=3\times10^{-4}$, $l=20$, $h=30$, $L=140$, $r_0=3$, $V=0.01$; (a) A and B fluids are nontransparent; (b) B fluid is transparent; (c) A fluid is transparent.

For relatively high values of the imposed velocity ($H\gg H_2=7\times10^{-4}$ for the parameters chosen here), the patches also switch the A and B fluid phases, but only near the patterned substrates. The morphology in the center of the channel ($z\approx h/2, y\approx h/2$) remains almost undisturbed. We observe a roughly 2×3 checkerboardlike design of A and B fluid phases at the outlet of the channel [similar to the snapshot of the morphology at the right end of the channel in Fig. 2(a)]. The exact morphology at the outlet is controlled by the value of the imposed pressure gradient, as well as by the fluid properties and the interaction with the substrates.

In both the limiting cases described above, the system exhibits a time-independent steady state. However, for the intermediate velocity region, $H_1\leqslant H\leqslant H_2$, we find surprisingly complex periodic behavior. Figure 2 depicts the morphology in the channel at late times for $H=3\times10^{-4}$; recall that the A fluid is shown in blue and the B fluid is shown in yellow. Figure 2(a) shows the channel as viewed from the side; in this image, the fluids are opaque and the behavior seems relatively simple. If, however, we look inside the channel and make one of the fluids transparent [the B fluid in Fig. 2(b) and the A fluid in Fig. 2(c)], we now see that an

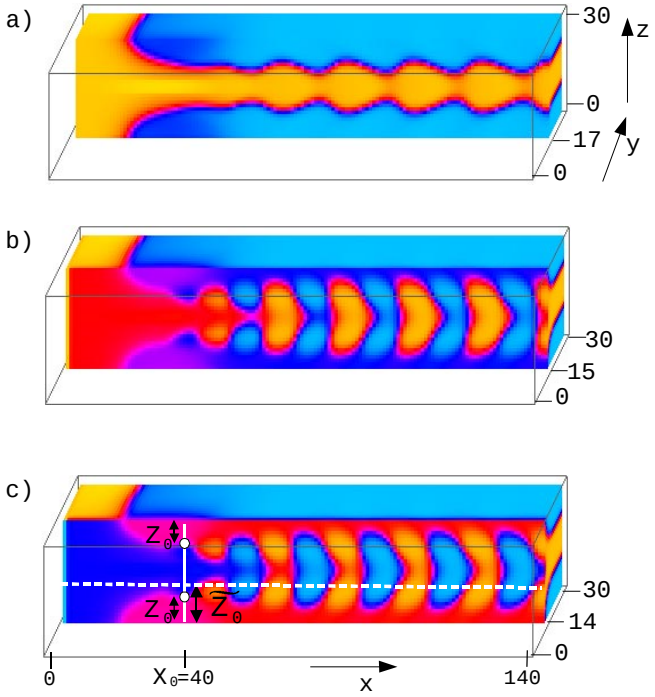

FIG. 3. (Color online) Order parameter distribution in a channel that is "cut" by vertical x-z plane at (a) $y=17$, (b) $y=15$, (c) $y=14$. The part of the channel in front of the cutting plane is transparent. The position of the end of the patches is $X_0=40$. All parameters are the same as in Fig. 2.

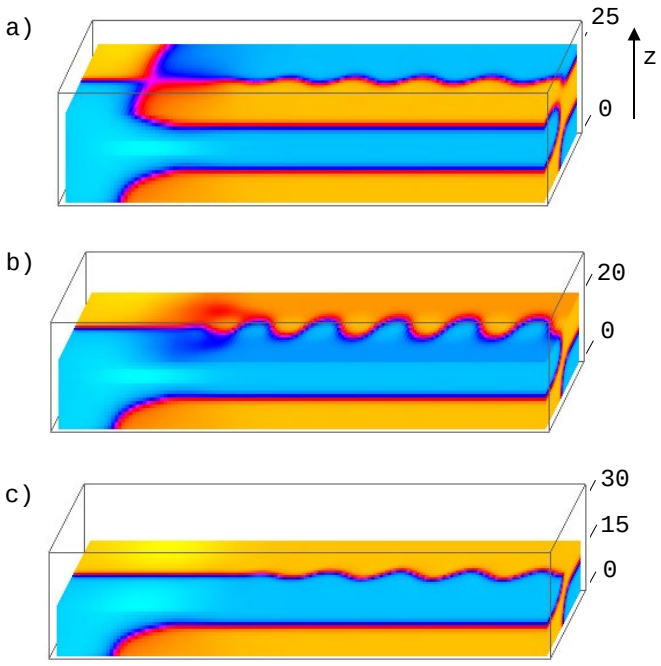

FIG. 4. (Color online) Order parameter distribution in a channel that is cut by horizontal x-y plane at (a) $z=25$, (b) $z=20$, (c) $z=15$. The part of the channel on the top of the cutting plane is transparent. All parameters are the same as in Fig. 2.

interpenetrating structure is formed, where the A and B fluid phases are intertwined.

Another way of viewing this structure is by looking at cross sections of the system in the x-z plane at fixed y, as in Fig. 3, or in the x-y plane at fixed z, as shown in Fig. 4. The amplitude of the oscillations in the x direction has a maximum value in the x-z plane close to the middle of the channel [Figs. 3(b) and 3(c)] and decreases close to the sidewalls [Fig. 3(a)]. With respect to the x-y plane, the amplitude of the wave in the y direction has a maximum value at some fixed distance from the substrates [Fig. 4(b)] and decreases at distances closer to the substrate [Fig. 4(a)] and in the middle of the channel [Fig. 4(c)].

If we examine the morphology as a function of time, we observe another unexpected feature of this system. This structure oscillates in time, so that the waves in Figs. 3 and 4 or the "holes" in Figs. 2(b) and 2(c) are seen to travel down the channel. The technologically most interesting case is the one shown in Fig. 3, where the moving waves can be regarded as sluglike flow. Here, the effect of the patches has been to switch two horizontal, parallel fluid streams to a stream of alternating, essentially vertical slabs of A and B phases near the center of the channel. The morphology at the outlet of the same channel evolves as shown in Fig. 5. The snapshots in this figure are taken over half of the temporal period; during the second half of the period, the system evolves from the morphology in Fig. 5(d) back to the morphology in Fig. 5(a).

To characterize the observed behavior, we measure the temporal period τ and the spatial period λ along the x axis down the channel. The value of τ can be measured from the time evolution of the order parameter at any point where oscillation occurs (there is a single frequency that describes the oscillations in time in our system). However, it is more difficult to measure the "wavelength" λ. For the case of small H, this value can be simply measured from the order parameter distribution along the x axis (downstream from the patterned region) for $y=h/2$, $z=h/2$ (in the center of the channel). For the case of high H, the oscillations have significant amplitude only close to the top and bottom substrates; the amplitude in the center of the channel ($y \approx h/2$, $z \approx h/2$) is very small. Therefore, for each value of H, it is reasonable to measure the spatial period along the line in the x direction where the oscillations are well established and the amplitude has the maximum value, namely, in the middle of the channel $y=y_0=h/2-1$ at the some distance $\tilde{Z}_0$ from the top or the bottom substrate. Specifically, we measure the spatial period λ from the order parameter distribution along the dashed line in Fig. 3(c).

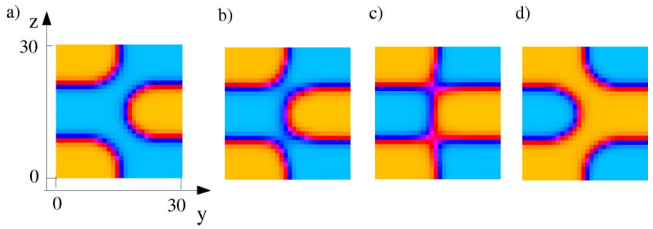

FIG. 5. (Color online) Morphology at the outlet of the microchannel for the simulation box shown in Figs. 3 and 4 but taken at different time steps: (a) $t=50\,100$, (b) $t=50\,400$, (c) $t=50\,500$, and (d) $t=50\,800$.

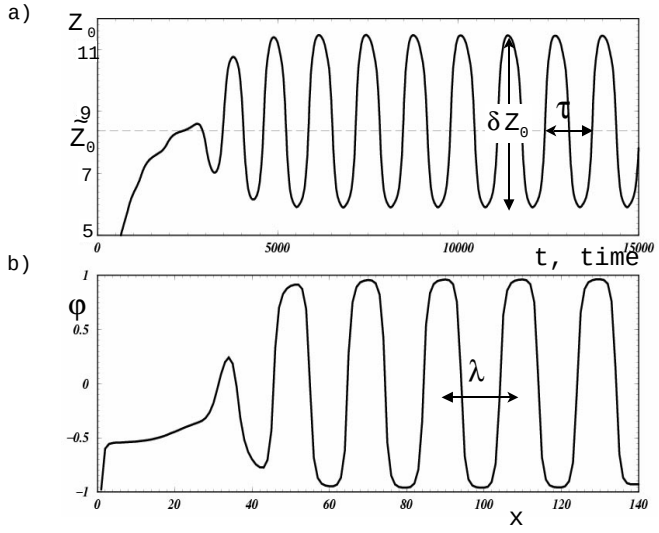

FIG. 6. (a) Evolution of Z_0 in time. (b) Order parameter distribution along x axis at $y=14$, $z=9$ at the time $t=6\times10^4$ time steps. All parameters are the same as in Fig. 2.

To define $\tilde{Z}_0$, first we locate the position of A/B interface, $Z(x,y)$, as the point(s) in z where the order parameter changes sign at fixed x and y. Specifically, we measure the position of the interface along the line located at the end of the patches and in the center of the channel along the y axis [solid white line in Fig. 3(c)]. In the simulation box, this position is denoted as $Z_0=Z(X_0,y_0)$, where X_0 is the position of the end of the patch [see Fig. 3(c)]. As can be seen from the morphology snapshots in Fig. 3, we have two A/B interfaces at $x=X_0,y\approx h/2$; the positions of these interfaces at fixed times are shown by white circles in Fig. 3(c). For simplicity, we assume that the value Z_0 is the distance from the bottom substrate to the nearest A/B interface; note that the distance from either the top or bottom substrate to the nearest interface is the same. The actual value of Z_0 is controlled by a competition between diffusion and advection due to the imposed velocity field.

As the intertwined structure is formed at the end of the patches, the value of Z_0 oscillates above and below its time average value $\tilde{Z}_0$. In the other words, if we examine the evolution of morphology shown in Fig. 3(c), we see the A/B interfaces (or white circles) oscillate up and down along the solid line. The actual time evolution of Z_0 is shown in Fig. 6(a). The dashed line in Fig. 6(a) shows the value of $\tilde{Z}_0$ for the above case. Both Z_0 and the peak-to-peak amplitude of the oscillations δZ_0 [Fig. 6(a)] depend on the imposed pressure gradient H. We measure the period in time τ from the data for the time evolution of Z_0 shown in Fig. 6(a). We measure the spatial period λ at the fixed time step from the order parameter distribution $\varphi(x,y_0,\tilde{Z}_0)$ in the middle of the channel $y=y_0$ at the distance $\tilde{Z}_0$ from the substrates as shown in Fig. 6(b).

As noted above, the spatiotemporal patterns that are formed in the channel depend on the magnitude of the imposed velocity. To explicitly illustrate this point, we show the structures for two different values of H (that are within the range $H_1\leqslant H\leqslant H_2$); the results capture the two different types of behavior that we observed in these studies. For relatively high velocities, as depicted in Fig. 7(a), the interpenetrating structures are formed near the top and the bottom substrates, but the morphology in the middle of the channel remains almost undisturbed. In one set of simulations, we removed the patches on the top substrate. In this case, we observe an intertwined structure that is similar to the one in Fig. 7(a), but the pattern only appears near the bottom (patterned) surface [Fig. 7(b)].

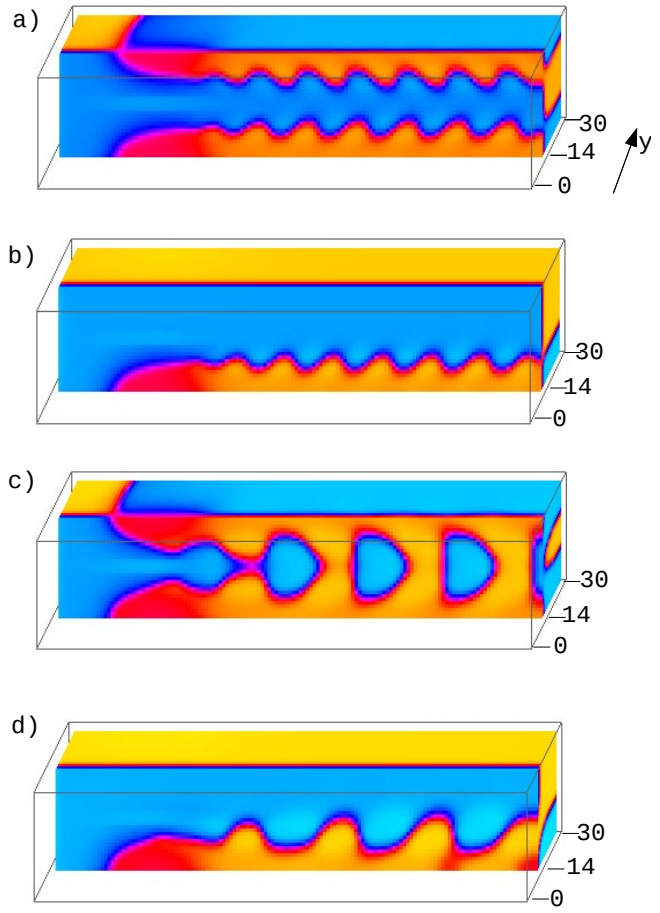

FIG. 7. (Color online) Order parameter distribution in a channel that is cut by vertical x-z plane at $y=14$. (a) $H=6\times10^{-4}$, patches are on the top and bottom; (b) $H=6\times10^{-4}$, patches are on the bottom only; (c) $H=3\times10^{-4}$, patches are on the top and bottom; (d) $H=3\times10^{-4}$, patches are on the bottom only.

For lower H, when the maximum value of Z_0 becomes comparable with $h/2$ (see Fig. 1), the structure that is formed close to the bottom substrate connects with the structure that is formed close to the top substrate [Fig. 7(c)]. As alluded to above, the flow down the middle of the channel now exhibits a sequential pattern of A/B/A/B . . . ''columns.'' To create this type of flow, it is necessary to have patches on both the top and bottom substrates of the channel. [If we have patches only on the bottom substrate, see Fig. 7(d), the spatiotemporal patterns will be similar to the ones observed, for example, in Fig. 7(b).]

In this essentially nonlinear, three-dimensional, finite-size problem, the stability analysis and the task of determining

analytically the frequencies corresponding to the oscillations in space and time is difficult. However, we propose simple scaling arguments that can help in elucidating the physics of the observed phenomena and also in predicting the complex spatiotemporal behavior. We begin with an analysis of the evolution in time of the A/B interface inside the patterned region. Specifically, at the distance approximately $\tilde{Z}_0$ from each substrate at the chosen probe point at the end of the patches [at the $x=X_0, y=h/2$ as shown on Fig. 3(c)], a relatively wide interface between the four fluid streams A/B/A/B is formed. The free energy favors the formation of large A (B) domains on the A-like (B-like) patches, or, in other words, a high value of Z_0. (For example, Z_0 takes its maximum value, $h/2$, at low velocities, where the fluid mimics the underlying patterns). Higher imposed velocities lead to lower values of Z_0; this value is limited from below by r_0, the range of the interaction with the substrate. The pattern formation described above happens at intermediate velocities, where $r_0 < \tilde{Z}_0 < h/2$.

The initiation of the pattern formation happens approximately at the distance $\tilde{Z}_0$ from the bottom (and at the same distance from the top substrate, simultaneously) as follows. First, the A (B) domains grow at the A-like (B-like) patches, and thus fluid phases are switched from their original path. At the end of the patches, and in the middle of the channel (at $y=h/2$), the tops of the A (B) domains extend into the bulk. The ''tops'' of these domains are in the path of the highest imposed velocity (since this is Poiseuille flow). Eventually, the A (B) tops are advected along by the imposed velocity and simultaneously diffuse back towards the main A (B) stream. Thus, the structures from both streams become intertwined as shown in Figs. 2–4.

Competition between the diffusive growth of the top region of an A (B) domain at the end of the patches and advection of this formation by an imposed velocity along the channel determines the spatial and temporal periods. We assume that the characteristic velocity that advects the structure along the channel is proportional to the velocity taken in the middle of the channel ($y \approx h/2$) and at the distance $\tilde{Z}_0$ from the substrate. Therefore we can relate the spatial and temporal periods as $\lambda/\tau \sim u(\tilde{Z}_0)$. Taking the effective radius of the top region of an A (B) domain to be proportional to the spatial period and assuming diffusive growth of this region, we can estimate the temporal period as $\tau \sim \lambda^3/\sigma$ [10]. Thus, the oscillations can be described by the two parameters:

$$\tau \sim \lambda/u(\tilde{Z}_0); \quad \lambda \sim \sqrt{\sigma/u(\tilde{Z}_0)}. \tag{7}$$

In these estimates, $\tilde{Z}_0$ still remains an unknown variable that can be estimated from the following simple argument. The characteristic time that is needed for fluid A to diffuse to the A-like patch, which is covered with an A layer of height $\tilde{Z}_0$, is proportional to $\tilde{Z}_0^2$ [17]. In order for this fluid to diffuse to the compatible domain, the advection time of a fluid element through the patterned region should be equal to or greater than the diffusion time estimated above. Recalling that l is the length of the patch, this condition can be written as $l/u(\tilde{Z}_0) \sim \tilde{Z}_0^2$, which gives a rough estimate of the steady-state value of $\tilde{Z}_0$. These estimates can strictly be used only if $r_0 \ll \tilde{Z}_0 \ll h/2$. For smaller $\tilde{Z}_0$, we should explicitly include the effective interaction with the substrate in the estimate; for higher $\tilde{Z}_0$, one should consider changes in the characteristic diffusive length. Taking the functional dependence of the velocity $u(\tilde{Z}_0) \approx H(h\tilde{Z}_0 - \tilde{Z}_0^2)/3.3$ from the Poiseuille flow [18], we can estimate the value of $u(\tilde{Z}_0)$ from the equation

$$H\tilde{Z}_0^2(h\tilde{Z}_0 - \tilde{Z}_0^2) \sim l. \tag{8}$$

Since $\tilde{Z}_0 \ll h$ (where h is the height of the channel), for simplicity we can neglect $\tilde{Z}_0^2$ in the formula above and find

$$\tilde{Z}_0 \sim \left(\frac{l}{Hh}\right)^{1/3}. \tag{9}$$

To test these scaling arguments, we carried out a specific series of simulations. In the first set, we ran the simulations for different values of H and measured the value of $\tilde{Z}_0$, as well as the spatial and temporal periods. In Fig. 8(a), we plot the simulation results for $\tilde{Z}_0$ (solid line with filled circles) for fixed values of l and $\tilde{\kappa}$, and the results calculated using Eq. (9) (dashed curve). Note that the available dynamic range is small since the observed phenomena occur in a relatively narrow parameter region. Due to this fact, an accurate verification of the scaling predictions from the simulation results is difficult if not impossible. However, we can compare the simulation results with the above estimates, taking reasonable numerical fitting parameters.We can see good agreement of the simulation results with the estimates for higher values of H and a noticeable discrepancy at lower values of H, as expected for the larger values of $\tilde{Z}_0$. Also in qualitative agreement with the above arguments, $\tilde{Z}_0$ remains roughly constant as we change the interfacial tension (by changing the value of $\tilde{\kappa}$). Figure 8(b) shows this behavior for two fixed values of H.

In the next series of simulations, we measure the dependence of $\tilde{Z}_0$ on the length of the patch for two fixed values of H [solid lines in Fig. 8(c)]. The dashed curves show the estimates using Eq. (9) [with the same value of the single fitting parameter that was used in Fig. 8(a)]. Thus, our assumptions prove to be fairly reasonable and Eq. (9) seems to capture the scaling behavior for $\tilde{Z}_0$ for the range of parameters considered here.

Using Eqs. (6) and (9), and taking $u(\tilde{Z}_0) \approx Hh\tilde{Z}_0/3.3$, we can estimate the full dependence of both the spatial and temporal periods on the system parameters:

$$\lambda \sim \frac{\sigma^{1/2}}{h^{1/3} l^{1/6} H^{1/3}}; \quad \tau \sim \frac{\sigma^{1/2}}{h l^{1/2} H} \quad (\text{''high H''}). \tag{10}$$

Figure 9(a) shows the dependence of the temporal period of the system's oscillations on the imposed pressure gradient. For relatively high velocities, there is an indication that the temporal period decays as $\tau \sim H^{-1}$, according to Eq. (10).

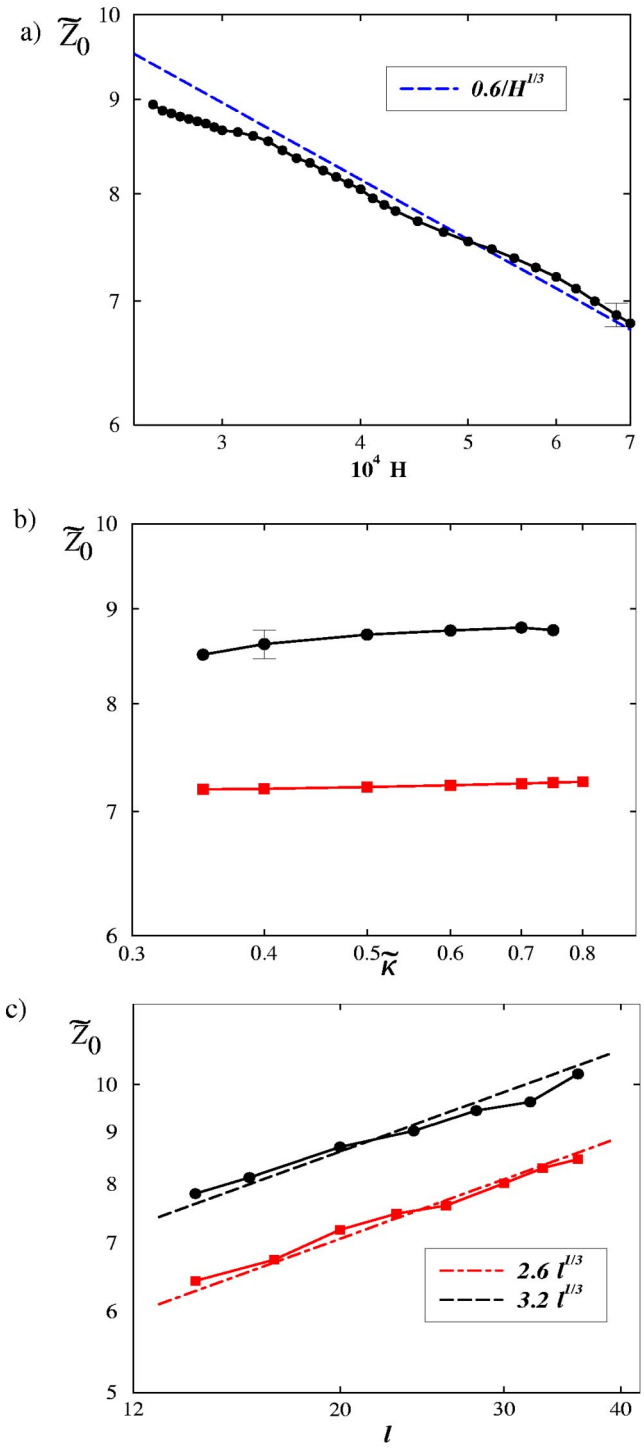

FIG. 8. (Color online) Dependence of $\tilde{Z}_0$ on (a) H for fixed $\tilde{\kappa}=0.5$, $l=20$; (b) $\tilde{\kappa}$ for fixed $H=3\times10^{-4}$ (curve with circles) and $H=6\times10^{-4}$ (curve with squares), $l=20$; (c) l for fixed $H=3\times10^{-4}$ (curve with circles) and $H=6\times10^{-4}$ (curve with squares), $\tilde{\kappa}=0.5$. Other parameters are the same as in Fig. 2.

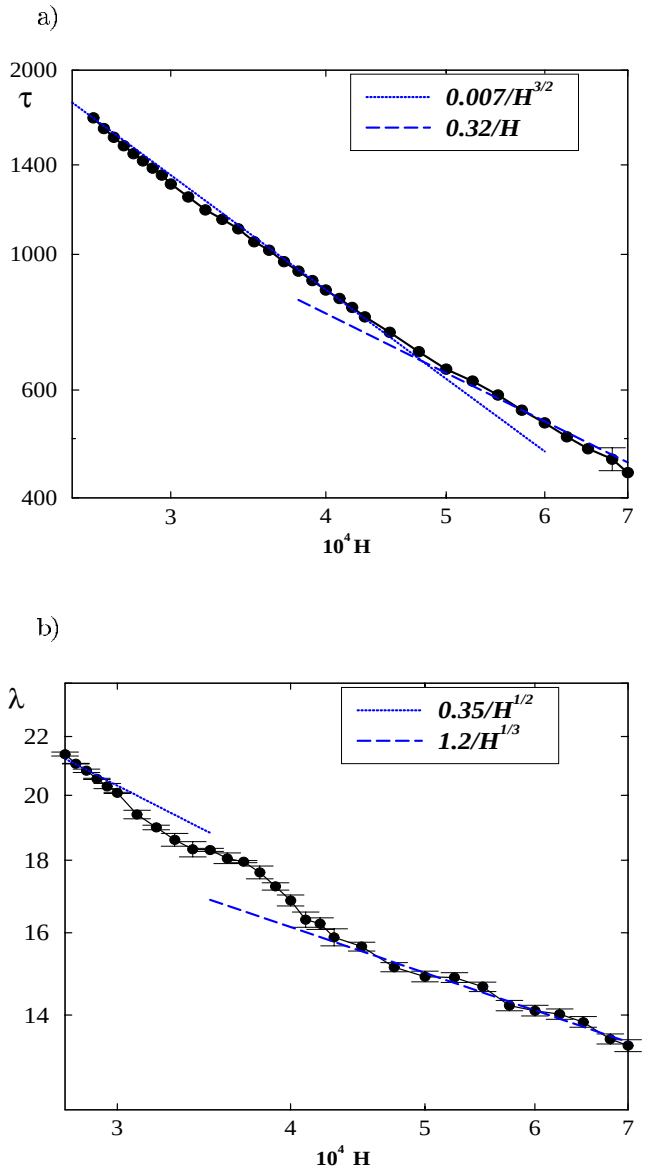

FIG. 9. (Color online) (a) Dependence of temporal period τ on H. Solid curve with the filled circles represent simulation results; dashed curve is an asymptotic form at high H, $\tau\approx0.32/H$; dotted curve is an asymptotic form at low H, $\tau\approx0.007/H^{3/2}$. (b) Dependence of spatial period λ on H. Solid curve with the filled circles represent simulation results; dashed curve is an asymptotic form for λ at high H, $\lambda\approx1.2/H^{1/3}$; dotted curve is an asymptotic form for λ at low H, $\lambda\approx0.35/H^{1/2}$. All other parameters are the same as in Fig. 2.

For the lower values of H, we see a significant deviation from H^{-1} behavior. The solid curve with the filled circles in Fig. 9(b) shows the spatial period along the x direction, λ, measured from the simulations at different values of H. Again, the above estimates of the spatial period from Eq. (10) are expected to apply only for relatively high values of H.

The reason for the deviation from the above estimates for low values of H is as follows. The amplitude of the oscillations of Z_0 increases with decreasing H; thus, the maximum value of Z_0 is close to $h/2$. In this case, the structures from the top and bottom merge. Therefore, the characteristic velocity that corresponds to the advection along the channel is no longer simply associated with $\tilde{Z}_0$, and is approximately equal to the velocity in the center of the channel, $u_{h/2}$

$=u_{max}\approx Hh^2/13$ [18]. Thus, using u_{max} instead of the $u(\tilde{Z}_0)$ in Eq. (6) leads to the following scaling estimates of periods for low H:

$$\lambda \sim \frac{\sigma^{1/2}}{hH^{1/2}}; \quad \tau \sim \frac{\sigma^{1/2}}{h^3 H^{3/2}} \quad (\text{“low H”}). \tag{11}$$

Using Eq. (11), we plotted the dotted curves in Fig. 9, which show the asymptotic behavior for lower values of H. The important qualitative feature of Eq. (11) is that the spatial and temporal periods do not depend on the length of the patch l for low H. However, the value of H where the crossover from the low-H regime [described by Eq. (11)] to the high-H [see Eq. (10)] occurs depends on l. As we decrease H further, or try to extend the simulation results (Fig. 9) to the region of still lower H, $H \leqslant H_1$, we also observe oscillations consistent with the scaling behavior of Eq. (11) at early times, but eventually these oscillations become unstable, indicating that the periodic state becomes unstable below our estimate of H_1.

In order to test the estimates further, we plotted the dependence of both the spatial and temporal periods on the value of $\tilde{\kappa}$ (the dimensionless interfacial tension in our model is $\sigma \sim \sqrt{\tilde{\kappa}}$) for two different values of H in Fig. 10. One value ($H=6\times10^{-4}$) is taken in the region of high H [solid curves with squares in Figs. 10(a) and 10(b)] and the other ($H=3\times10^{-4}$) is taken from the region of low H [solid curves with circles in Figs. 10(a) and 10(b)]. For the larger value of H, the estimates from Eq. (10) are consistent with the simulation results (see dashed-dotted lines in Fig. 10), and correspondingly, we used estimates from Eq. (11) for the case of $H=3\times10^{-4}$. It is encouraging that the simulations indicate roughly the same $\tilde{\kappa}$ dependence in the “low H” and “high H” regimes.

Though not shown here, we also find from the simulations that the dependence of the spatial and temporal periods on the patch lengths agrees with Eqs. (10) for the high H region. In the low H region, the spatial and temporal periods do not depend on the patch length, as consistent with Eq. (11).

Thus, Eq. (10) allows us to estimate relatively accurately the spatial and temporal periods in the case of relatively high velocities, where the traveling waves that occur near the top and the bottom substrate are separated by a relatively undistorted two-stream flow in the middle of the channel. For the low velocities, where the traveling wave disturbances from the top and the bottom merge, both the spatial and temporal periods increase more rapidly with decrease in H, according to Eq. (11). In both situations, the established intertwining structures travel down the channel with the phase velocity λ/τ.

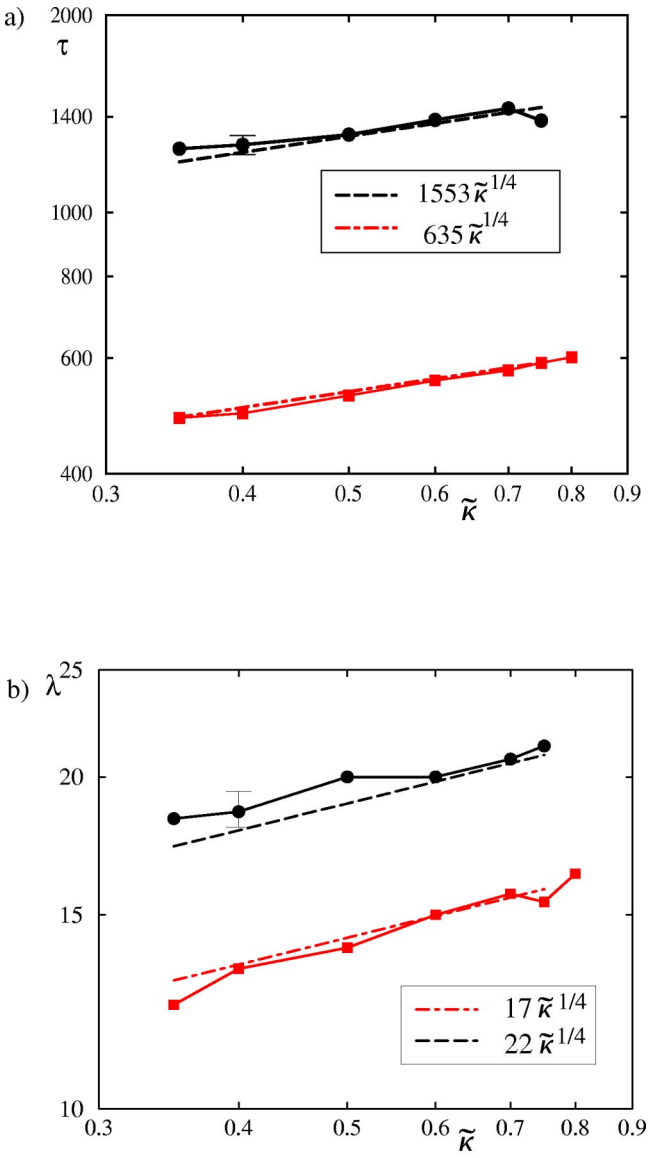

FIG. 10. (Color online) (a) Dependence of the temporal period τ on $\tilde{\kappa}$. Solid curve with the filled circles represents simulation results for $H=3\times10^{-4}$; dashed curve represents an asymptotic form for this case, $\tau\approx1553\tilde{\kappa}^{1/4}$. Solid curve with the filled squares represents simulation results for $H=6\times10^{-4}$; dashed-dotted curve represents an asymptotic form, $\tau\approx635\tilde{\kappa}^{1/4}$. (b) Dependence of the spatial period λ on $\tilde{\kappa}$. Solid curve with the filled circles represents simulation results for $H=3\times10^{-4}$; dashed curve represents an asymptotic form for this case, $\lambda\approx22\tilde{\kappa}^{1/4}$. Solid curve with the filled squares represents simulation results for $H=6\times10^{-4}$; dashed-dotted curve represents an asymptotic form, $\lambda\approx17\tilde{\kappa}^{1/4}$. All others parameters are the same as in Fig. 2.

IV. CONCLUSIONS

The simulations show oscillatory pattern formation as two immiscible fluids A and B flow through a microchannel that contains chemically distinct patches on the top and bottom substrates. The patches are designed to have a preferential attraction to the A or B fluid. The A-like (B-like) patch is placed in the path of the B (A) fluid. The observed spatiotemporal patterns fall onto two distinct categories, exhibiting different scaling behavior as we change system parameters. For relatively high velocities, oscillatory structures are formed near the top and the bottom substrates, but the morphology in the middle of the channel remains almost undis-

turbed. The same oscillations occur if we have patches only on the top or the bottom substrate. The periods in time and space decrease with increases in H as $\tau \sim 1/H$ and $\lambda \sim 1/H^{1/3}$, respectively.

For the region of relatively low velocities, the structures that are formed close to the top and bottom substrate grow large enough to become entangled with one another. In this case, the flow down the channel may be regarded as sluglike flow, where two parallel fluid streams are switched to the sequential A/B/A/B . . . streams. To create this type of flow, it is necessary to have patches on both the top and bottom substrates of the channel. In this case, the periods in time and space show a more rapid increase with decreasing H, namely, as $\tau \sim 1/H^{3/2}$ and $\lambda \sim 1/H^{1/2}$, respectively.

We also estimated the dependence of spatial and temporal periods on the length of the patches and on the interfacial tension between fluids. Thus, it is possible to control the oscillations by changing the imposed pressure gradient H for the fluid with the chosen interfacial properties.

The simple design of the chemically modified patches proposed here can be used to redirect the flow of fluids in microchannels, switching the two parallel A/B streams to B/A streams for low values of the imposed velocities. In addition, the pattern can be used to generate sluglike flow from the two parallel streams. We find that the complex behavior in such a relatively simple system arises from the competition between advection and thermodynamically driven diffusion as an imposed flow drives fluids to move over the patches on the substrates. This concept can be exploited to design surface patterns that will yield new dynamical behavior [9] and can be useful in controlling the mixing of binary fluids [7,8] or the motion of droplets in microfluidic devices.

ACKNOWLEDGMENTS

The authors acknowledge support from the ONR and NSF.

[1] J.M. Ottino, *The Kinematics Of Mixing: Stretching, Chaos and Transport* (Cambridge University Press, Cambridge, 1989).
[2] M.C. Cross and P.C. Hohenberg, Rev. Mod. Phys. **65**, 851 (1993).
[3] M. Husemann *et al.*, JACS **122**, 1844 (2000).
[4] N. Abbot *et al.*, Science **257**, 1380 (1992).
[5] R. Blossey, Nat. Mater. **2**, 301 (2003).
[6] B. Zhao, J. Moore, and D.J. Beebe, Science **291**, 1023 (2001).
[7] O. Kuksenok, J.M. Yeomans, and A.C. Balazs, Phys. Rev. E **65**, 031502 (2002).
[8] O. Kuksenok and A. Balazs, Phys. Rev. E **68**, 011502 (2003).
[9] O. Kuksenok, D. Jasnow, J.M. Yeomans, and A. Balazs, Phys. Rev. Lett. **91**, 108303 (2003).
[10] A.J. Bray, Adv. Phys. **43**, 357 (1994).
[11] We ignore a model-dependent dimensionless coefficient of order unity and use this expression for the interfacial tension.
[12] A.C. Balazs *et al.*, J. Phys. Chem. B **104**, 3411 (2000).
[13] D. Jasnow and J. Vinals, Phys. Fluids **8**, 660 (1996)
[14] H-Y. Chen, D. Jasnow, and J. Vinals, Phys. Rev. Lett. **85**, 1686 (2000).
[15] Y. Oono and S. Puri, Phys. Rev. A **38**, 434 (1988)
[16] We introduce noise in the strength of the interaction at each point of the checkerboard pattern, i.e., $V(\vec{s}) = V(1 + 0.01\zeta(\vec{s}))$, where the independently distributed random numbers $\zeta(\vec{s})$ lie in [-1 1).
[17] Recall that in dimensionless units the chemical potential is $\mu = -\varphi + \varphi^3 - \tilde{\kappa}\nabla^2\varphi + \delta\Psi_s/\delta\varphi$. The charactersistic time τ_0 for the diffusion of an order parameter fluctuation through the lengh scale $\tilde{Z}_0$ can be obtained from the analysis of Eq. (3), which gives $\varphi/\tau_0 \sim \varphi/\tilde{Z}_0^2$; thus $\tau_0 \sim \tilde{Z}_0^2$.
[18] The exact solution of $\nabla^2 u_x + H = 0$ with boundary conditions $u_x|_{z=0} = u_x|_{z=h} = 0$, $u_x|_{y=0} = u_x|_{y=h} = 0$ gives $u_x = \Sigma_{n=1}^{\infty}\Sigma_{m=1}^{\infty}[4Hh^2/\pi^4 mn(m^2+n^2)\sin(m\pi y/h)]\sin(n\pi z/h)$, where n and m are odd numbers. In the simulations, we truncate the sum at $n = m = 35$. For the fixed value of $y = h/2$, the above sum can be numerically approximated as $u_x = u(z) \approx H(hz - z^2)/3.3$. The velocity at the center of the channel, $y = h/2, z = h/2$, can be approximated as $u_{\max} \approx Hh^2/13$.